A test rig for the validation of CFD simulations of a passenger vehicle under hood environment

Case Studies in Thermal Engineering 59 (2024) 104423

Contents lists available at ScienceDirect

Case Studies in Thermal Engineering

journal homepage: www.elsevier.com/locate/csite

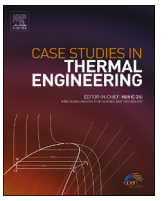

A test rig for the validation of CFD simulations of a passenger vehicle under hood environment

Alexey Vdovin [a, *], Tarun Kadri Sathiyan [a], Christophe Duwig [b], Ammar Hazim Saber [a]

[a] Chalmers University of Technology, Sweden
[b] KTH Royal Institute of Technology, Sweden

ARTICLE INFO

Handling Editor: Huihe Qiu

Keywords:
Engine test rig
Testing
CFD
Thermal management
Underhood flow
PIV

ABSTRACT

As part of global efforts to reduce greenhouse gas emissions, the automotive industry is moving towards the electrification of its fleet – including full electric and hybrid vehicles. Considering hybrid vehicles, the energy efficiency and thermal management of powertrains including IC engines remains an important contribution. In this regard, engineers need accurate tools to understand heat-transfer in engine bays. This work presents a flexible test rig design to be used for the validation of CFD simulations of an underhood environment. The test rig and measurement equipment are introduced in detail with experimental data (and CAD) being available.

A possible test scenario presented in this research is when an engine is subjected to heavy loads (i.e., constant uphill driving) and the vehicle is subsequently stopped. The experimental results are analysed and, furthermore, the data in terms of flow and temperature fields is compared against the results of the numerical simulations. This sort of comparison is the main usage scenario for the constructed rig, and it demonstrates the value of this facility for research. The rig's geometry and the experimental data being available can additionally be used to facilitate development and validation of various CAE methodology as well as simulation techniques.

1. Introduction

Sustainable transport is a key to creating a sustainable society. The International Energy Agency (IEA) reports that buses and trucks emit 2.2 GT CO_2 per year [1] and foresee a reduction to 2 GT CO_2 by 2030. The reduction is mostly for medium duty trucks (−25 %) while heavy duty is decreasing by 8 %. Realistic paths to reduce the emissions include switching fuels, electrification, and gains in efficiency. The latest includes vehicle efficiency technologies, systemic improvements in logistics and supply chain operations, and environmental policy tools [2].

Focusing on technical progress, the deadline calls for shorter development times from the concept phase to the final product. To achieve this, a reduction of expensive and lengthy physical testing is necessary to facilitate faster deliveries to the market. To guarantee proper product development, virtual methods can be used instead. They offer the benefit of being less costly and have a faster turnaround time. However, their benefit is conditioned to having a verified and validated procedure. In this work, a physical test rig is designed and constructed with the objective of increase the understanding and improve the simulation modelling that will, in turn, accelerate the development of new generation clean vehicles.

Focusing on the engine compartment, a significant air flow rate passes through the compartment and is used to cool the engine and evacuate the waste-heat from the engine. This results in an aerodynamic loss which is referred as cooling drag in the literature

* Corresponding author. Chalmers University, Horsalsvagen 7A, M2 Department, 412 58, Goteborg, Sweden.
E-mail address: alexey.vdovin@chalmers.se (A. Vdovin).

https://doi.org/10.1016/j.csite.2024.104423
Received 4 August 2023; Received in revised form 8 December 2023; Accepted 18 April 2024
Available online 27 April 2024

[3,4]. It consists of pressure drop over specific component, secondary flows in the engine bay or modification of the external aerodynamics, e.g., Ref. [5]. The relative importance of the cooling drag compared to the total drag varies depending on the engine load and vehicle design. Some studies provide a quantification of the contribution to the total drag of the order of 30–60 counts (ΔC_D = 0.03–0.06) [3], which corresponds to 7–10 % of the overall drag [6,7].

The state-of-the-art for engine bay cooling research includes using Computational Fluid Dynamics (CFD) simulations to analyse and optimize the flow of air through the engine bay, for example [8–11]. This includes studying the effects of different fan configurations, ducting designs, and grille openings on the cooling performance. These works were focused on developing more energy efficient cooling systems and on reducing the aerodynamic drag caused by these systems. For instance, the use of active grill shutters that can adjust the airflow based on the engine's cooling needs, as well as the use of more aerodynamic shapes for the ducting and grille openings. While these avenues are attractive, the CFD tools require a thorough validation by comparison with detailed and relevant experimental data obtained from wind tunnel tests or on-vehicle testing. This includes comparing the predicted airflow patterns, temperature distributions, and pressure drops to the corresponding measurements from the experiments.

One of the specific challenges in validating CFD simulations for engine bay cooling is accurately modelling the complex geometry of the engine bay and the various components within it [8–11]. Wang et al. [8] presented a comparison of RANS and LES turbulence models for simulating the flow in a steady-state engine cooling system, using wind tunnel experimental data for validation. The study found that both RANS and LES models were able to predict the mean flow characteristics of the cooling system, but the LES model provided more accurate predictions of the turbulent flow structures.

Zhang et al. [9] reported experimental and numerical study of an engine cooling system, using wind tunnel testing and CFD simulations to investigate the effect of different grille opening sizes and shapes on the cooling performance. The study used RANS turbulence model and found that the simulation results were in good agreement with the experimental data. Yang et al. [10] also presented a comparison of RANS and LES models with similar conclusions. This offers a good base for increasing the level of complexity – for looking at unsteady cases. In fact, challenges in engine bay cooling simulations lie in the complexity of the system. The geometrical data (component geometries and locations) are usually known - not perfectly though - but the non-geometrical data (conductivity of rubber, surface emission index, aging effects ….) are often partly unknown. The level of details of these approaches might vary (e.g., Ref. [12]) but have in common a relative lack of comprehensive validation and verification. There is a strong need for research towards developing validation and verification strategies based on reliable experimental validation data.

Test rigs for automotive aerodynamics have been suggested in the literature, the two prominent being the Ahmed body [13] and the DrivAer [14]. The first has been used extensively to test CFD and turbulence models. The relative simplicity of the external flow has enabled laser diagnostics and provided a detailed database with velocity fields. Several attempts were made to include internal flow features but without geometries relevant to engine bay configurations. The specificities of engine bay flow and heat-transfer lies in the multiphysics and complex aspects of the problem, including multiple components (radiators, fans, …) with a non-trivial behaviour [15]. Firstly, the heat-transfer regime is mixed, ranging from pure natural convection (soak, immobile vehicle) to force convection at high vehicle speed. Intermediate regimes include fan-driven cooling for cars. Traditional investigations of complete vehicles enable to quantify globally the cooling drag and even test the influence of different features for drag reduction, e.g. Refs. [6,7,16–22]. However, these studies use global or point measurements and do not provide detailed information for extensive CFD verification and validation. In addition, they often report steady experiments while the critical moments for real vehicles are transient (e.g., soak, start/stop, …).

Khaled et al. [23] have classified the different phenomena of importance in the engine compartment, namely: (i) the complex internal airflows in the compartment, and (ii) the aerodynamic interaction between the internal and external airflows and its impact on the aerodynamic drag. (ii) has been partly investigated experimentally in DrivAer-like configurations and to some extends by traditional investigation (see references above). (i) has been less studied but has direct value for model verification and CFD methods validation. Literature data reporting the internal air flows are sparse. Merati et al. [24] have studied the buoyant flow in a simplified engine bay model. Although the geometry was severely simplified, the detailed velocity measurements enabled CFD performance validation [25–28]. Khaled et al. [23,29] have discussed the issue of building a more detailed engine compartment model that is realistic enough to be of interest and simple enough to enable detailed measurements. Another rig with slightly better optical access was presented by Franzke et al. [30]. However, both these rigs having a relatively more detailed geometry, investigated only the aerodynamic aspect of the underhood environment without any thermal characteristics.

These studies made clear that the next step in validation of CFD for engine bay investigation called for an optically accessible test rig consisting of adequate detailing in the geometry that provides an opportunity of combined aerodynamic and thermodynamic investigations. A good illustration for such a test rig was presented by Sweetman et al. [31].

This article presents a new test rig to study and model engine bay aerodynamic and thermal flows. The rig design is discussed in detail with explanations of all components involved. These components are built to be generic and not specific to any vehicle. They are described sufficiently along with all the necessary details which allow the rig geometry to be used in research with a possibility to reproduce the results. Some of the components are also modular, allowing for various designs to be analysed. The rig's geometry and the experimental results being available can be used in research and facilitate CAE method development of simulation techniques.

To demonstrate the possible use case scenario of the rig, an example experimental procedure is also presented in detail. The results are shown, discussed and, furthermore, compared to CFD simulations. The authors' aim is to demonstrate the value of the presented rig and experimental data for validation of CFD simulations.

2. Experimental setup

2.1. Test rig description

The test rig featuring a simplified, but relevant vehicle engine bay, is shown in Fig. 1. The rig is designed and constructed with the aim to study the aerodynamic flows along with thermal conditions under the hood. The rig consists of hot and cold parts, ceramic heaters, radiators, an electrical fan, and a water jacket. The entire setup is enclosed using special borosilicate glass walls which are held by a support structure made of aluminium. The support structure raises the rig setup off the floor, isolating it from vibration and heat conduction to the surroundings. The borosilicate glass panels are used to withstand high thermal stresses that they are subjected to during the tests. The glass walls provide access for optical measurements (i.e., PIV) through the rig. The fan drives the air through the inlet, the air passes around various parts and exits through the three outlets, one on either side of the rig and another at the rear.

The hot parts consist of a catalyst, a collector, a manifold, an exhaust pipe, and a turbo. All these components are made of copper. All the hot parts are embedded with several ceramic cartridge heaters as shown comprehensively in Fig 19, Appendix B. These heaters are inserted into the openings that are precisely reamed to dimension. To optimize metal-to-metal contact, mitigate corrosion, and safeguard against heating element deterioration, a thermally conductive paste has been employed. Additionally, during operational conditions, the heaters undergo faster expansion relative to other components, effectively occupying any remaining gaps and ensuring appropriate thermal contact. The control of the heaters is done through PWM switching by a solid-state relay, controlled through a LabView program. The control loops for PID controllers use the maximum temperature from the group of heaters as feedback. However, to ensure the safety of operations, ramping up of the target temperatures is performed manually in several increments. Accuracy of control should correspond to the accuracy of the K-type thermocouple, which is also the only signal input to the controller.

The cold parts, made of aluminium, mainly consist of an engine block, a circular and a rectangular cylinder, and a heat shield, which are shown in Fig 18, Appendix B. Inside the engine block, a water jacket is installed to ensure that the rear of the engine block (which is in close proximity to the hot parts) does not exceed a temperature of 100 °C. At the front end of the test rig, there is a fan along with two radiators placed before and after the fan. The fan drives the air through the rig enclosure and one of the radiators functions as a flow straightener to decrease the amount of rotational momentum of the flow inside the rig.

2.2. PIV (particle image velocimetry)

Fig. 2 shows a schematic diagram of the PIV setup which is used to study the flow distribution around hot parts of the test rig. The setup primarily consists of a light source (i.e., laser), high-resolution camera, laser sheet optics, tracer or seed particles and a data acquisition system. The domain of interest is infused with tracer particles which are suspended in the incoming flow. A laser sheet is used to illuminate the tracer particles in a selected plane of interest at frequent time intervals with the help of light sheet optics. A combination of cylindrical and spherical lenses controls the sheet thickness and location. Furthermore, a high-resolution camera is utilised to capture the frame for analysis. The laser and the high-resolution camera are synchronised through a microprocessor that is sequentially rigged to a computer.

Twelve vertical planes in lateral direction are accessible to cover the volume of interest and each plane consisting of six field of views (FOVs) in vertical direction and three in horizontal. Each FOV has a dimension of 114 × 86 mm and every one of these sections partially overlap with every other by approximately 4.5 mm in either direction as shown by the magnified image in Fig. 2. All these FOVs are later stitched together to obtain the flow field for individual measurement planes. Additionally, three horizontal planes in vertical direction are analysed which is similarly divided into three FOVs in horizontal direction and eight in lateral.

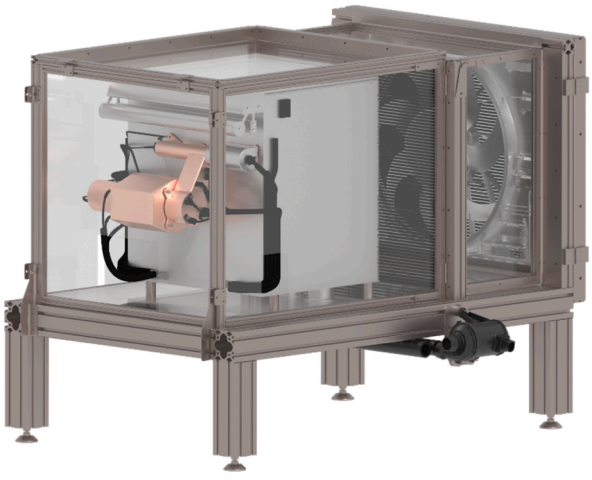

Fig. 1. An illustration of the test rig.

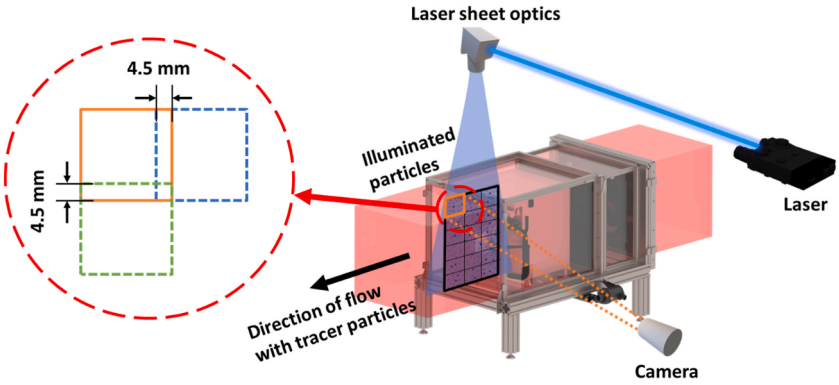

Fig. 2. Schematic diagram of PIV setup.

2.3. *Temperature measurements*

The surface temperatures of key locations are measured using 66 K-type thermocouples labelled as TK1 to TK66. Thermocouples TK1 to TK15 are present in hot parts, cold parts are represented by TK16 to TK32. The thermocouple tips are inserted into pre-drilled holes of an appropriate diameter in the corresponding parts. The contact (interference) fit is achieved by at least 3 centerpunches close to each hole. This approach is chosen to immobilize the thermocouple as well as maintain contact between its tip and the metal surface. TK33 to TK49 correlate to the internal heater temperatures. The rest of the thermocouples are used for monitoring temperatures of the glass walls, engine block and water temperature. The temperature measurement uncertainly for the TKs used is equivalent to the uncertainly of the probe along with the added uncertainly from the signal conditioning hardware as well as the datalogger (i.e., PC-Logger 2100 [32]) that it is connected to. In this case, the measurement uncertainty is estimated to be about 6° for the TKs operating at temperatures of around 700 °C. Two examples of the thermocouple installation into catalyst, the exhaust pipe and the collector are as shown in Fig. 3. A detailed description of the exact positions of the thermocouples in the CAD model can be found in Appendix A.

3. Experimental procedure

The entire experimental procedure can be divided into two phases, namely, heat-up phase and cool-down phase as shown in Fig. 4.

Fig. 3. Examples of thermocouples embedded into catalyst and the exhaust pipe.

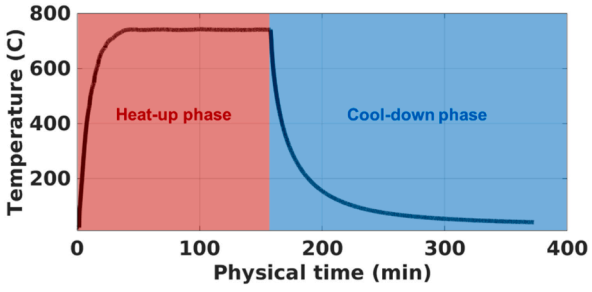

Fig. 4. An illustration of heat-up (and stabilization) and cool-down phases in an experimental test run.

3.1. Heat-up phase

This is the phase when the heaters are switched on, to start heating up all the copper parts. The air flow through the rig is induced by the fan throughout the heating phase. The ceramic heaters are manually controlled in groups. Furthermore, the groupings are based on the hot parts i.e., 2 heaters in the manifold, 6 heaters in the catalyst, 3 heaters in the collector, 3 heaters in the exhaust pipe and 3 heaters in the turbo which summate to five groups in total. The heaters in each of the five groups are of different sizes which is based on the target temperature as well as the overall dimensions of each copper part.

A target heater temperature per group is used as a control for the entire system. The target temperatures for the heaters in catalyst and exhaust pipe are 580 °C, and for the turbo, collector and manifold they are 740 °C per part, hence, the temperature levels are realistic and are sufficient to induce natural convection. The amount of power supplied to every group of heaters is controlled manually based on instantaneous temperature readings from the heaters. When one of the heaters in each of the five groups report reaching the target temperature, the heating and the fan are turned off. This is the start of the soaking phase. It should be noted that due to the limited number of heaters per part and different external conditions on various surfaces, the attained surface temperatures per part are non-uniform, which is to be expected. The same is true for the heater temperatures within the corresponding group of heaters. For example, after the heat-up phase is complete, the heater in the exposed manifold is on average 26 °C cooler than the heater on the other side of the manifold that is partially covered by the heat shield.

3.2. Cool-down phase

At the start of cool-down phase, all the heaters are switched off and the fan is stopped ensuring that there is no forced convection. It mimics the engine stop and the heat-transfer is driven by natural convection and radiation. Throughout this phase, the thermocouples continuously monitor the surface temperatures of all the parts in the test rig. The heat in the system is dissipated via natural convection and radiation through the glass panels.

4. Numerical setup

Numerical simulations are performed with the aim designing better engine bays and thermal protection. The philosophy is to reproduce the flow field sufficiently well to enable an accurate heat-transfer prediction.

4.1. Rig model and mesh

The simulation model of the rig enclosure is shown in Fig. 5. The two radiators are highlighted in yellow; air outlets are represented in red, hot parts are coloured as copper and all cold parts are shown as silver. To account for the heat conduction inside parts, all solid objects except the fan are simulated as solid regions and have solid mesh inside them. A cut through the computational domain showing the mesh is seen in Fig. 6. As indicated by colours, the domain is split into regions to better control different settings and the mesh. Fluid (air) regions are connected using internal interface boundaries (e.g., openings connecting the air inside the rig and the outer domain). Fluid to solids use mapped-contact interfaces.

Most of the air regions are meshed using hexahedral cells and have 1 to 3 prismatic layers next to the surfaces to capture accurately the gradients in the boundary layer. The only air region with a different cell type is the fan, where blade rotation is simulated using multiple reference frame (MRF) and, hence, polyhedral cells are preferable to better-accommodate non-unidirectional flows [33]. As for the solid regions, they are mostly meshed using polyhedral mesher to make sure there are at least 5 cells through the depth of thin parts to be able to effectively capture the temperature gradients inside.

To ensure the boundary conditions of the outer boundaries in the computational domain would not influence the flow around the test rig, the size of the computational domain is chosen to be sufficiently large. The dimensions are as shown in Fig. 7. The floor and sides of the domain are simulated as walls with a constant temperature of 28 °C while the top of the domain is assigned a pressure outlet boundary condition allowing a backflow of air with the same temperature. This is done to account for the ventilation system posi-

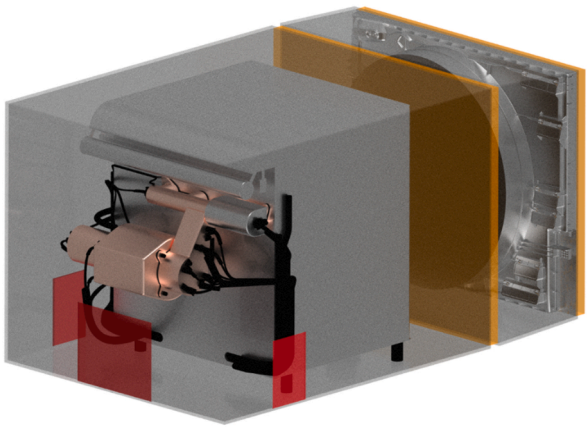

Fig. 5. Test rig geometry with radiators highlighted in yellow and air outlets highlighted in red.

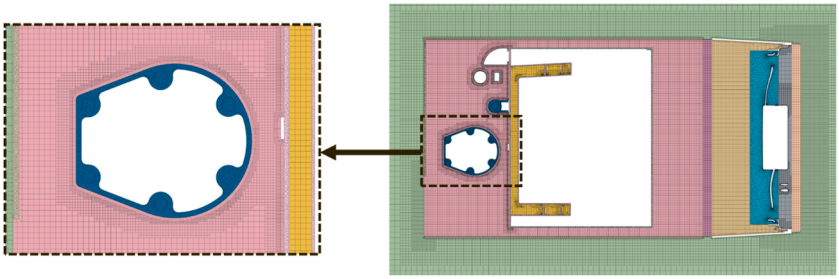

Fig. 6. A section cut through the mesh at the centreline of the rig.

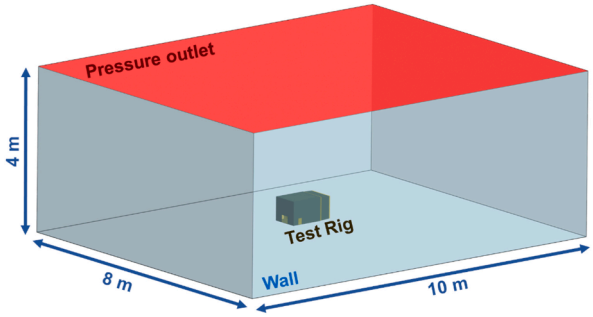

Fig. 7. Size of the computational domain and boundary conditions.

tioned on top of the rig during the experimental testing. A temperature of 28 °C is chosen as it is an average air temperature measured in the room while the tests are conducted. Internal walls within the parts that do not have thermal interfaces to the air (i.e., boundaries connected to the unmeshed internal volumes) are simulated using adiabatic boundaries. The heat is introduced to the domain with a volumetric heat flux applied equally to all heaters within their corresponding groups.

To secure a mesh independence of the solution, a mesh study is performed in different regions of the computational domain. The final mesh resulted in around 14 M fluid cells and 7 M cells for solids. A more detailed description of different regions, and how they are setup, can be found in Appendix B.

4.2. Simulation setup for rig components

Starting at the front of the test rig, both the pre-radiator and radiator are commercially produced heat exchangers, therefore, they are both simulated as porous regions with known inertial and viscous air resistance curves. As mentioned, the fan region is simulated using MRF approach with a rotational rate of 2000 rpm. This rotational velocity, together with the pressure drop through the radiators, resulted in a total mass flow rate of air through the rig during the heat-up phase to be 0.513 kg/s.

As all the cold parts are constructed using aluminium and, hence, their solid representation is assigned to the same material properties in the numerical setup. All hot parts are assigned as copper with the corresponding material properties. In reality, all the solids (hot parts) along with the engine block contains air trapped inside them. However, this internal air does not interfere with external surroundings. Therefore, the inner air volumes are not meshed, and the interior walls of these solids are prescribed to an adiabatic boundary condition. Heaters are simulated as solid ceramics with a thermal contact resistance introduced between them and the hot parts. The value of 6.0E-4 m^2K/W is calculated based on the heater manufacturer estimation of the temperature difference between the heater and the hot part surface right next to it [34]. A different contact resistance of 1.0E-4 m^2K/W is additionally introduced in the spots where collector is welded to the manifold and turbo. The rest of the contacts between parts have isolating materials and, thus, they are not modelled as contact interfaces in the simulation.

The glass panels which are made up of borosilicate glass requires using multiband thermal radiation model for the simulations. This is due to transmissivity and emissivity of these glass panels are strongly dependent on wavelength. As for the other surfaces, emissivity of aluminium parts is set to 0.1 and copper parts is set to 0.5 in the simulation model.

Lastly, the water region inside the engine block is modelled as a solid body with material properties of water – since the water flow is zero during the experiments. The inner wall of the water chamber which is further away from the hot parts is assigned to have a static temperature measured from the water tank at the end of the heat-up phase.

4.3. Description of the two phases of the test

As the tests contain two phases (heat-up and cool-down), the physics setup is slightly distinct. For the heat-up phase, the experimental tests are performed with gradual increase in the heater temperatures using manual control of the heaters. Even though the final temperatures for the heat-up phase are close to each other for repetitions of the same test, the presence of a manual control leads to significant differences in heat-up curves. Therefore, it is decided not to simulate the transient heat-up phase and focus on obtaining

the right airflow and temperature distribution inside the rig after an equilibrium condition is reached, before starting of the cool-down phase. Consequently, the heat-up phase is simulated using steady-state Reynolds-Averaged Navier-Stokes (RANS) with an ideal gas model for air and realizable k-epsilon model for turbulence.

The solution obtained from the steady state simulation is used as a starting point for the soak (cool-down phase). To initiate soak conditions, the energy supply to the heaters is assigned as 0 and the fan is completely stopped. It is assumed that apart from a limited time at the beginning of cool-down phase, the soak is not a truly transient flow case. Consequently, a semi-transient approach is applied. Flow changes occur due to changes in temperature field. This means that updating the flow field at certain time intervals to compensate for changes in temperature is necessary. Between these occasions, the flow can be frozen and only the energy equation is resolved with a much larger time step. To summarize, the first minute is simulated using unsteady RANS (URANS) when both flow and energy are resolved. The rest of the soak is progressed in a manner of only unfreezing the flow solver once in 2 s to update the flow field, as represented in Fig. 8.

5. Results and discussions

This section summarizes the outcomes of the experimental measurements and makes a comparison with the simulation results. To simplify analyses for the temperature measurements, only the thermocouples on the metal parts are be considered. These thermocouples are the most significant for the analyses as they are located on the hot and cold parts of the rig.

5.1. Experimental repeatability

To study the experimental repeatability of the results, the same test is performed five times. Part surface temperatures reported by thermocouples after the heat-up phase and standard deviation of the measurements are shown in Fig. 9.

While minor discrepancies are present in between curves, they still agree reasonably well, especially for hot parts (TK1-TK15) and particularly for the catalyst and the exhaust pipe (TK9-TK15). Cold parts (circular and rectangular rods, TK16-TK21) also show good repeatability with differences below 5 °C. Surface temperatures of the engine block (TK22-TK32) show the most deviations between experiments, which can be explained by the fact that some of the tests are ran consecutively and the water inside the cooling jacket,

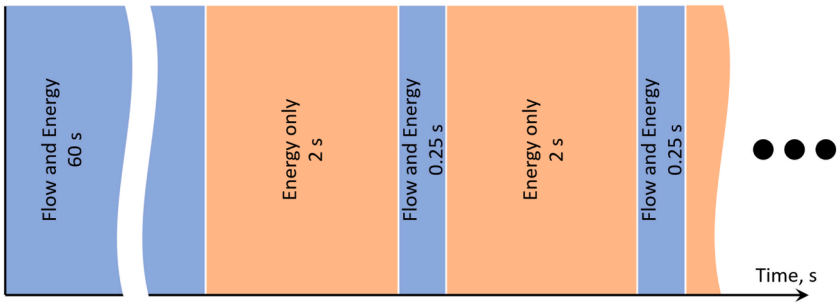

Fig. 8. Simulation timeline.

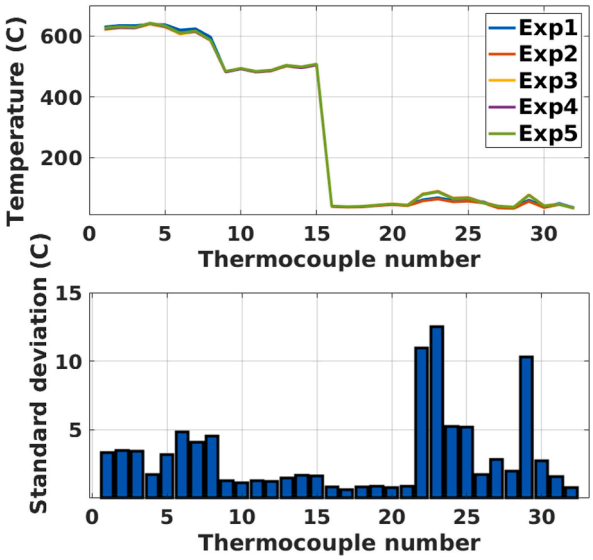

Fig. 9. Plot with thermocouple temperatures before start of soak for all test runs with corresponding standard deviation.

being a large thermal mass, did not have enough time reach an equilibrium state. However, these differences are small compared to the temperature variations in the system.

To have a benchmark temperature value of every thermocouple, experimental average is considered for all further assessments.

5.2. Comparison of flow features between simulation and experiments using PIV

To demonstrate the capabilities for validation of flow field in the geometry, PIV and CFD results are compared. For the purpose of this paper, only four planes are considered since they provide sufficient information of the flow characteristics. The planes are labelled A, B, C, D positioned at 374, 231, 131, 31 mm respectively from the inner surface of the glass which is depicted by a reference line (dashed line) as shown in Fig. 10. The results presented below represent the averaged flow field when the fan is running, and the heaters switched off. This illustrates cold flow in the domain without any thermal interference.

Fig. 11 indicates the coherence between various flow features captured by simulations in terms of velocity plots versus experimental PIV. The arrows indicate flow directions and colours represent mean velocity for the velocity components tangential to the planes. Firstly, a complex flow pattern with bottom-up flow driven by convection is observed. The resulting vortices are constrained by the geometry. An imbalance with stronger flows in the region of higher temperature can be noticed. Planes A and B

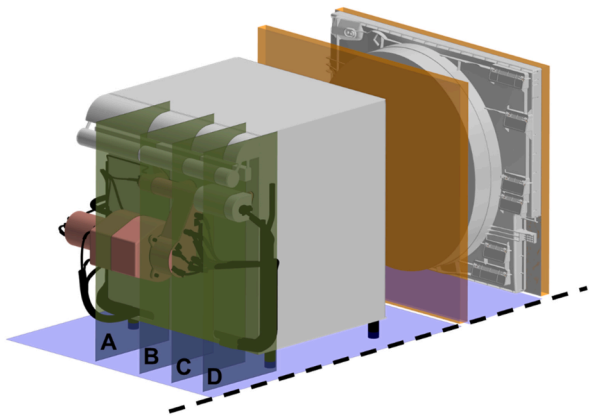

Fig. 10. PIV planes used for comparing PIV data to cold-flow simulation results.

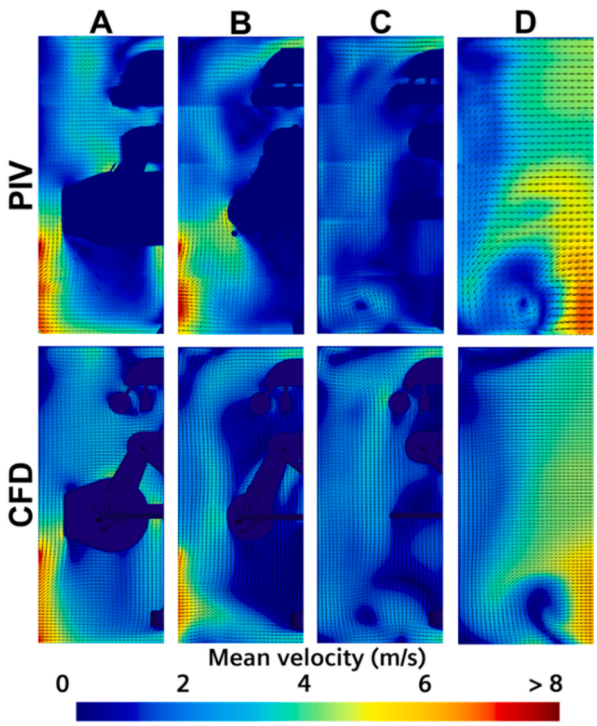

Fig. 11. PIV and CFD results for the four section planes.

show analogous flow accelerations around the hot parts between PIV and simulations. Distinctive large energetic vortex structures are seen in plane C (bottom left) and plane D (bottom). The comparisons indicate that the CFD approach used captures qualitatively the flow dynamics. For more detailed comparison DES or LES methods should be used.

5.3. Comparison of part temperatures at the start of soak

Fig. 12 represents the surface temperatures of different parts after the steady-state heat-up simulation, just before the start of the soak i.e., end of the first phase. The objective is to capture quantitatively the temperature levels in the engine compartment and at critical locations.

At the end of phase one when the heating phase has reached a seemingly steady state, thermocouple temperatures of both hot parts (TK1-TK15) and cold parts (TK16-TK32) are compared against its corresponding experimental averages. Fig. 13 validates that the thermocouple temperatures at the start of cool-downs are consistent relative to the experimental average.

As to be expected, there are minor variations for some of the TKs, but the overall surface temperature distribution is captured very well. This shows that the method can predict surface temperature at critical locations within less than 10 °C discrepancy. This confirms that the CFD method can help engineers to prevent overheating of sensitive components and design adequate engine compartments.

5.4. Transient soak simulations

Fig. 14 denotes the stages of natural convection plume formation for the first 50 s after start of soak. The air temperatures at the start of cool down are indicated at 0 s, which is right after the heaters are turned off and the fan is stopped. As the cold air is no longer forced through the fan, the air surrounding the hot parts becomes warmer and starts to rise due to buoyancy. This can be seen at 10 s. Furthermore, at 20 s the natural convection plume starts to form and the air around the hot parts starts to rise as it carries energy from the hot parts that is to be dissipated to cool it down. Cooler air then starts entering the rig from the outlets and engulf-

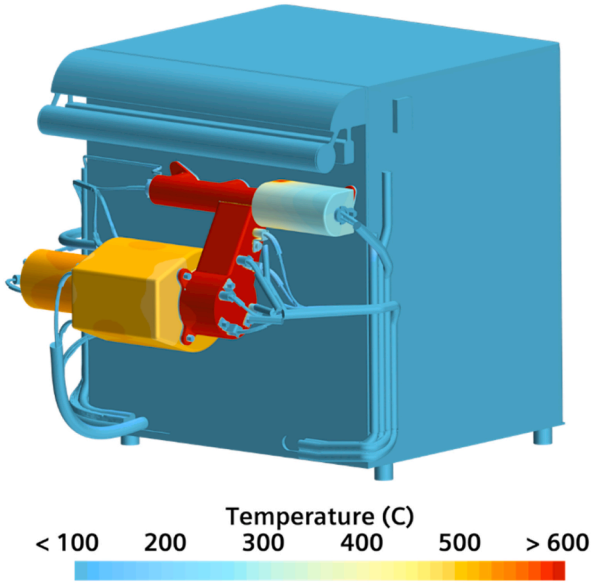

Fig. 12. Part temperatures in the beginning of a cool-down phase.

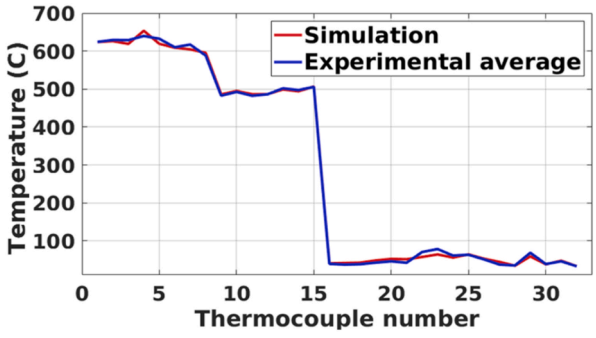

Fig. 13. Plot comparing average experimental thermocouple temperatures against simulation before start of soak.

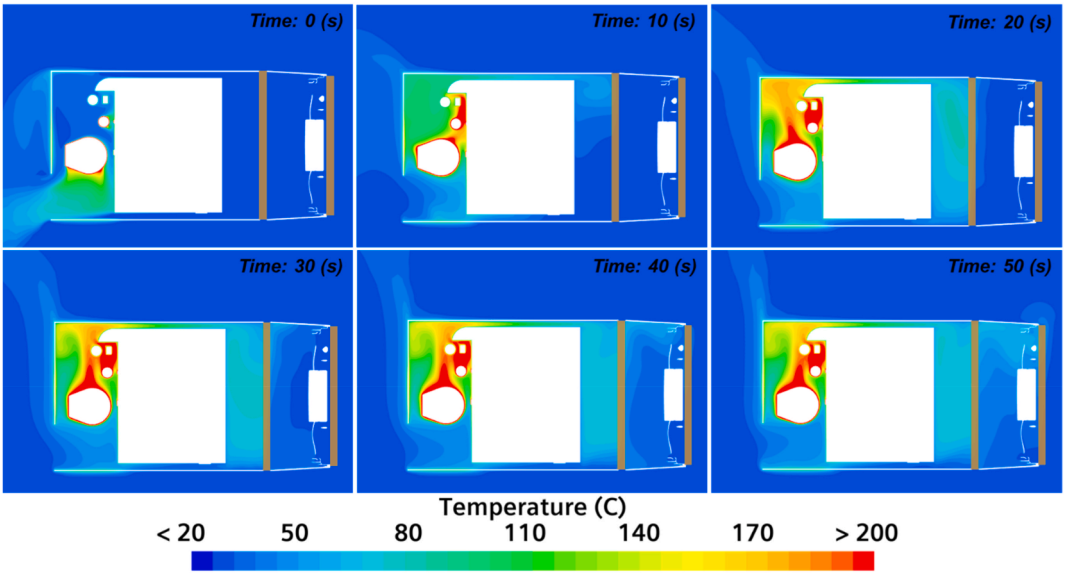

Fig. 14. Stages of natural convection plume formation.

ing the hot parts from underneath which is seen at 30 s. This phenomenon continues as the average air temperature inside the rig increases causing the cold parts and glass walls to heat up while hot parts cool down.

At 40 and 50 s, as the openings of the rig are positioned lower than the top part of the radiator (see Fig. 5), the buoyancy effect leads the air to escape through the radiators highlighted brown in the figure.

5.5. Comparison study of transient cooldown curves

To showcase some of the results a quantitative comparison of cool-down curves for 2 TKs from hot parts and 2 TKs from cold is presented in Figs. 15 and 16, respectively. Temperatures of the hot parts drop at the start of soak when the heaters are turned off and the fan stopped. Whereas temperatures of the cold parts rise for a few minutes to a relatively higher temperature before they start to drop. The reason for this is that during heat-up phase, the cold parts are exposed to forced convection by the cold air, hence, the surface temperatures are kept low. However, as the fan is stopped, the air temperature around these parts rises rapidly due to a hot plume formation shown in Fig. 14.

It is evident that the cool down curves from simulation corelate well with that of the experimental average for hot parts. These comparisons show that the method captures well the thermal inertia of the system and the heat-flux from the hot parts. The curves for the cold parts, while being more apart, have similar slopes compared to the experimental average. The slope for the temperature in-

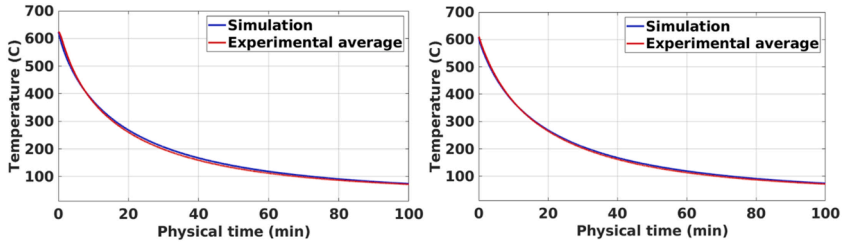

Fig. 15. Cool down curves of hot parts: TK1 (left) and TK6 (right).

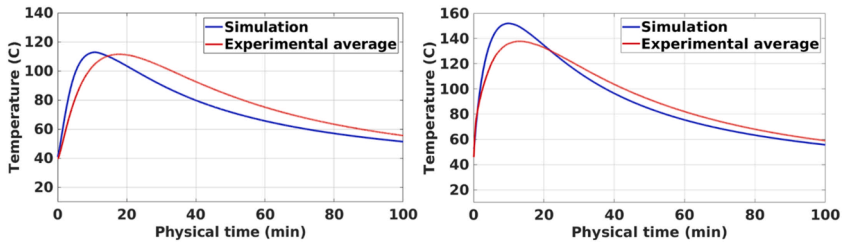

Fig. 16. Cool down curves of cold parts:TK16 (left) and TK20 (right).

Table 1
Max temperatures and average difference in peak temperatures for cold parts.

TK No.	Max temperature, °C (Simulation)	Max temperature, °C (Experimental average)	Temperature difference, °C	Average temperature difference, °C
16	112.9	111.5	+1.4	8.6
17	131.4	115.6	+15.7	
18	125.5	116.9	+8.6	
19	122.6	127.6	−5.0	10.4
20	152.0	137.8	+14.2	
21	154.5	142.6	+11.9	

crease is slightly faster in the simulations and thereby reaches a higher maximum temperature. The temperature decrease is simulated well with a predicted temperature drop slope close to the measured one. The simulations over-estimate the peak temperatures by less than 20 °C. In fact, the simulations present a "worst-case" scenario compared to the experiments and are still valuable for design engineers that are assessing the need for heatshield installations on exposed parts. It should also be noted that there is a clear difference seen on the time scales of the figures for cold and hot parts overexaggerating the difference in temperatures. Table 1 summarizes maximum temperatures of all cold part TKs from the simulation compared to the averaged value obtained from the experiments. The maximum differences for both the cylindrical and rectangular rods are obtained in the middle of these parts, however, the total averaged temperature difference does not exceed 9.5 °C.

6. Conclusions

In this work, a modular engine bay test rig for flow and heat transfer investigations is designed and built with the purpose of generating results for CFD validation. The rig allows to carry out experimental measurements of velocimetry and temperatures in geometries which are representative of close to realistic automotive underhood flow conditions.

To demonstrate the possible use case of the test rig, one such practical scenario where underhood parts heat-up while driving followed by the vehicle standing still and soaking, is presented in the paper. As a result of the executed experiments, a significant amount of data is generated in terms of PIV measurements and surface temperature measurements. A subset of this data is described and investigated. The results obtained are compared to CFD simulations which validated the temperature fields as well as the flow field within the test rig. Hence, demonstrating the value and capabilities of the test rig.

The flow prediction to qualitatively validate the transport predictions, and the temperature measurements to quantitatively validate the surface temperatures are used. In general, the flow is well captured and enables good predictions of convective heat-transfer. The surface temperatures of the hot parts are also well captured, even during transient cooling. The temperature of the cold parts exhibited a transient temperature increase before cooling. The characteristic time scales of the temperature increase are over-estimated by the simulations. As a result, the peak temperature is higher. However, the over-estimation is below 20 °C, which is an acceptable accuracy for design engineers securing material resistance.

The rig's geometry combined with the experimental results being available can be applied in research to facilitate development as well as validate various CAE methods and simulation techniques. This paper only presents a small part of the total result database. A more complete experimental data set including the CAD of the rig can be made available upon request.

CRediT authorship contribution statement

Alexey Vdovin: Conceptualization, Data curation, Formal analysis, Investigation, Methodology, Resources, Supervision, Validation, Visualization, Writing – original draft, Writing – review & editing. **Tarun Kadri Sathiyan:** Conceptualization, Data curation, Formal analysis, Investigation, Methodology, Validation, Visualization, Writing – original draft, Writing – review & editing. **Christophe Duwig:** Conceptualization, Project administration, Supervision, Writing – original draft, Funding acquisition. **Ammar Hazim Saber:** Data curation, Formal analysis, Investigation, Methodology.

Declaration of competing interest

The authors declare that they have no known competing financial interests or personal relationships that could have appeared to influence the work reported in this paper.

Data availability

Data will be made available on request.

Acknowledgements

The computations were enabled by resources provided by the National Academic Infrastructure for Supercomputing in Sweden (NAISS) and the Swedish National Infrastructure for Computing (SNIC) at National Supercomputer Centre (NSC) and Chalmers' Centre for Computational Science and Engineering (C3SE) partially funded by the Swedish Research Council through grant agreements no. 2022–06725 and no. 2018–05973.

The authors would like to acknowledge Volvo Car Corporation as well as Volvo Truck Technology for their significant contribution into designing and building the rig.

Lastly, financial support for the studies was provided by Strategic Vehicle Research and Innovation (FFI) under project number P44920-1.

Appendix A

TK #	Description	X, mm	Y, mm	Z, mm
TK1	Manifold, top, left	1624	-52	760
TK2	Manifold, top, middle, left	1624	7	760
TK3	Manifold, top, middle	1624	82	760
TK4	Manifold, top, right	1624	218	760
TK5	Manifold, front, middle	1602	81	740
TK6	Collector, rear, centre line, close to turbo weld	1683	82	674
TK7	Collector, front, centre line, close to manifold weld	1613	82	707
TK8	Turbo, bottom, centre line	1652	83	577
TK9	Catalyst, rear flat surf, right, close to symmetry plane	1770	29	622
TK10	Catalyst, rear flat surf, middle, close to symmetry plane	1770	-46	602
TK11	Catalyst, left surface, rear, close to upper heater	1755	-101	628
TK12	Catalyst, right surface, rear, at symmetry plane	1755	50	628
TK13	Catalyst, top, left	1682	-61	680
TK14	Catalyst, top, right	1654	23	675
TK15	Pipe	1646	-213	626
TK16	Circular cylinder, rear, left	1685	-208	824
TK17	Circular cylinder, rear, middle	1685	-3	824
TK18	Circular cylinder, rear, right	1684	168	824
TK19	Rectangular cylinder, rear, left	1626	-208	825
TK20	Rectangular cylinder, rear, middle	1626	2	825
TK21	Rectangular cylinder, rear, right	1626	168	825
TK22	Engine box, rear side, close to catalyst	1581	-68	659
TK23	Engine box, rear side, close to manifold	1581	85	699
TK24	Engine box, rear side, close to pipe	1581	-145	549
TK25	Engine box, rear side, close to turbo	1581	85	549
TK26	Engine box, rear side, lower right corner	1581	235	439
TK27	Engine box, top, centre line, rear	1566	55	909
TK28	Engine box, top, centre line, middle	1423	55	909
TK29	Engine box, right side, at manifold height, rear	1560	255	739
TK30	Engine box, right side, at manifold height, middle	1421	255	739
TK31	Engine box, bottom, at centreline, rear	1561	20	389
TK32	Engine box, bottom, at centreline, middle	1371	20	389
TK33	Heater manifold 1	1622	-1	740
TK34	Heater catalyst 6	1632	-28	643
TK35	Heater catalyst 5	1632	-28	577
TK36	Heater catalyst 1	1693	-28	667
TK37	Heater catalyst 4	1693	-28	553
TK38	Heater catalyst 2	1759	-28	643
TK39	Heater catalyst 3	1759	-28	577
TK40	Heater pipe 3	1657	-168	595
TK41	Heater pipe 1	1682	-168	639
TK42	Heater pipe 2	1707	-168	595
TK43	Heater manifold 2	1622	164	740
TK44	Heater collector 1	1639	91	704
TK45	Heater collector 2	1641	91	656
TK46	Heater collector 3	1673	91	671
TK47	Heater turbo 2	1649	94	602
TK48	Heater turbo 1	1711	94	628
TK49	Heater turbo 3	1696	94	579
TK50	Glass sheet, inner side, rear 1	1822	-240	901
TK51	Glass sheet, inner side, rear 2	1822	33	812
TK52	Glass sheet, inner side, rear 3	1822	-207	625
TK53	Glass sheet, inner side, rear 4	1822	4	652
TK54	Glass sheet, inner side, rear 5	1822	91	670
TK55	Glass sheet, inner side, rear 6	1822	256	518
TK56	Glass sheet, inner side, top 1	1569	-194	933
TK57	Glass sheet, inner side, top 2	1755	21	933
TK58	Glass sheet, inner side, top 3	1650	21	933
TK59	Glass sheet, inner side, top 4	1422	21	933
TK60	Glass sheet, inner side, top 5	1536	182	933
TK61	Glass sheet, inner side, right 1	1727	344	865
TK62	Glass sheet, inner side, right 2	1368	344	783
TK63	Glass sheet, inner side, right 3	1684	344	665
TK64	Glass sheet, inner side, right 4	1564	344	684
TK65	Glass sheet, inner side, right 5	1765	344	484
TK66	Glass sheet, inner side, right 6	1564	344	512

Appendix B

Following is a list of the most important settings for different parts of the simulated rig.

1. Glass walls:

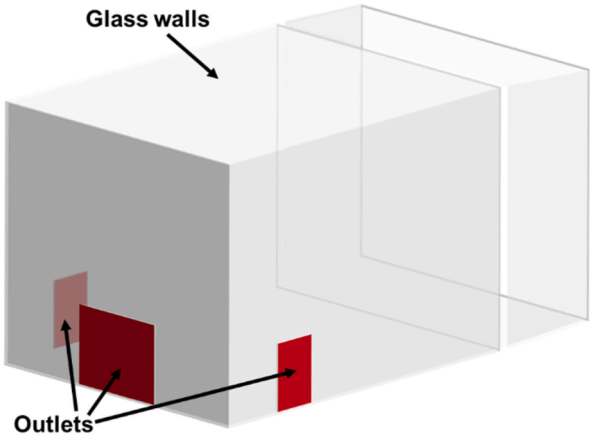

Fig. 17. Borosilicate glass walls with rig outlets highlighted in red.

Borosilicate glass panels, shown in Fig 17, are simulated.

2. Cold parts:

All metal parts of the rig that did not have heaters inside, see Fig 18, are simulated as hollow aluminium shells with a surface emissivity of 0.2. All inner walls are assigned with adiabatic boundary conditions. The only aluminium part that is not hollow, the heat shield, is just simulated as sheet metal.

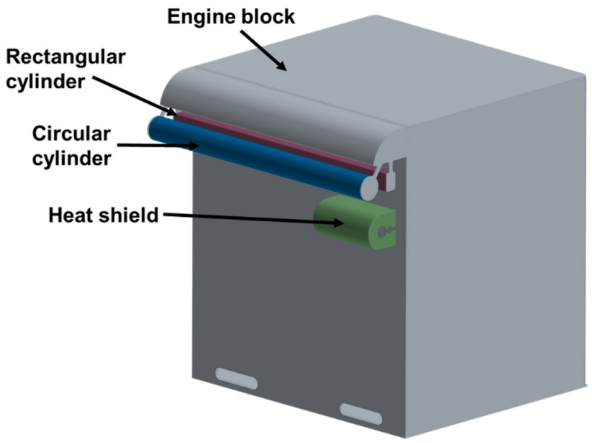

Fig. 18. Cold parts.

3. Hot parts:

The copper parts that represented simplified manifold, collector, turbo, catalyst, and exhaust pipe, as shown in Fig 19, are simulated in a similar way compared to cold parts. Material is copper, 0.5 for surface emissivity.

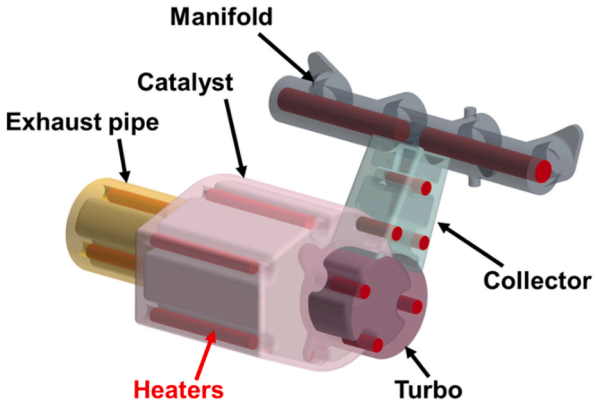

Fig. 19. Hot parts.

Inside the hot parts in the same figure one can see the positions of heaters. These heaters are simulated as completely solid ceramic rods.

4. Other parts:

Other important parts of the rig can be found in Fig 20. As mentioned in the main article text, the fan is simulated using MRF approach, and the radiators are modelled as porous media regions. Lastly, the water jacket while originally simulated as fluid region in the final model is represented by solid mesh with water properties and the back wall assigned with the water temperature measured during the experiments.

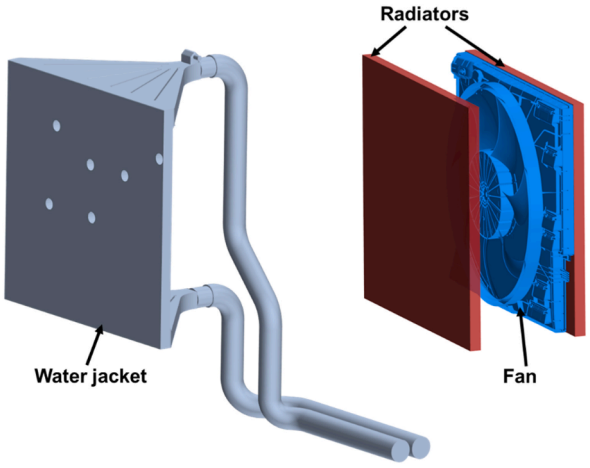

Fig. 20. Other parts.

References

[1] Trucks & buses - Fuels & Technologies - IEA." Accessed: November. 23, 2023. [Online]. Available: https://www.iea.org/fuels-and-technologies/trucks-buses.
[2] The Future of Trucks – Analysis - IEA." Accessed: November. 23, 2023. [Online]. Available: https://www.iea.org/reports/the-future-of-trucks.
[3] V. Renn, A. Gilhaus, Aerodynamics of Vehicle Cooling Systems, 1986.
[4] T.C. Schuetz, Aerodynamics of Road Vehicles, fifth ed., 2015, https://doi.org/10.4271/r-430.
[5] T. Ohshima, K. Hamatani, M. Ninoyu, K. Nakagawa, Influence of the cooling air flow outlet on the aerodynamic characteristics, JSAE Rev. 19 (2) (Apr. 1998) 137–142, https://doi.org/10.1016/S0389-4304(97)00064-7.
[6] P. Gilliéron, F. Chometon, Reduction of cooling air drag of road vehicles: an analytical approach, SAE Technical Papers (2001), https://doi.org/10.4271/2001-01-1266.
[7] H. Jama, S. Watkins, C. Dixon, Reduced drag and adequate cooling for passenger vehicles using variable area front air intakes, SAE Technical Papers (2006), https://doi.org/10.4271/2006-01-0342.
[8] Z. Wang, J. Han, D. Mukutmoni, Numerical simulation of unsteady natural convection in a simplified engine bay enclosure under soak conditions, in: *SAE Technical Papers*, SAE International, 2014, https://doi.org/10.4271/2014-01-0651.
[9] C. Zhang, M. Uddin, A.C. Robinson, L. Foster, Full vehicle CFD investigations on the influence of front-end configuration on radiator performance and cooling drag, Appl. Therm. Eng. 130 (Feb. 2018) 1328–1340, https://doi.org/10.1016/j.applthermaleng.2017.11.086.
[10] X. Yang, S. Gupta, T.W. Kuo, V. Gopalakrishnan, RANS and LES of IC engine flows: a comparative study, ASME 2013 Internal Combustion Engine Division Fall Technical Conference, ICEF 2013 2 (Feb) (2014), https://doi.org/10.1115/ICEF2013-19043.

[11] S. Kula, E. Bulut, E. Altay, O. Sümer, F. Oztürk, Smart cooling design using dual loop cooling to increase engine efficiency and decrease fuel emissions with artificial intelligence, Case Stud. Therm. Eng. 40 (Dec. 2022) 102351, https://doi.org/10.1016/J.CSITE.2022.102351.
[12] H.R. Shim, J.M. Park, A study of the transient analysis technique on the under hood thermal damage. SAE Technical Papers, 2011, https://doi.org/10.4271/2011-28-0126.
[13] Ahmed body -- CFD-Wiki, the free CFD reference." Accessed: November. 23, 2023. [Online]. Available: https://www.cfd-online.com/Wiki/Ahmed_body.
[14] DrivAer - Chair of Aerodynamics and Fluid Mechanics." Accessed: November. 23, 2023. [Online]. Available: https://www.epc.ed.tum.de/en/aer/research-groups/automotive/drivaer/.
[15] M. Khaled, F. Mangi, H. El Hage, F. Harambat, H. Peerhossaini, Fan air flow analysis and heat transfer enhancement of vehicle underhood cooling system – towards a new control approach for fuel consumption reduction, Appl. Energy 91 (1) (Mar. 2012) 439–450, https://doi.org/10.1016/j.apenergy.2011.10.017.
[16] R.H. Barnard, Theoretical and experimental investigation of the aerodynamic drag due to automotive cooling systems 214 (8) (Aug. 2000) 919–927, https://doi.org/10.1177/095440700021400810.
[17] J. Williams, Aerodynamic drag of engine-cooling airflow with external interference, in: SAE Technical Papers, 2003, https://doi.org/10.4271/2003-01-0996.
[18] D. Baeder, T. Indinger, N. Adams, P. Unterlechner, Aerodynamic investigation of vehicle cooling-drag. SAE Technical Papers, 2012, https://doi.org/10.4271/2012-01-0170.
[19] T. Hobeika, S. Sebben, L. Löfdahl, Experimental and numerical investigations of cooling drag, Proc. Inst. Mech. Eng. - Part D J. Automob. Eng. 231 (9) (Aug. 2017) 1203–1210, https://doi.org/10.1177/0954407016684740.
[20] T. Hobeika, P. Gullberg, S. Sebben, L. Lofdahl, Force based measurement method for cooling flow quantification, SAE International Journal of Passenger Cars - Mechanical Systems 10 (2) (Mar. 2017) 619–627, https://doi.org/10.4271/2017-01-1520.
[21] L. Larson, S. Woodiga, R. Gin, R. Lietz, Aerodynamic investigation of cooling drag of a production sedan Part 1: test results, SAE International Journal of Passenger Cars - Mechanical Systems 10 (2) (Mar. 2017) 628–637, https://doi.org/10.4271/2017-01-1521.
[22] L. Larson, R. Gin, R. Lietz, Aerodynamic investigation of cooling drag of a production sedan Part 2: CFD results, SAE International Journal of Passenger Cars - Mechanical Systems 10 (1) (2017) 214–223, https://doi.org/10.4271/2017-01-1528.
[23] M. Khaled, M. Ramadan, H. El-Hage, A. Elmarakbi, F. Harambat, H. Peerhossaini, Review of underhood aerothermal management: towards vehicle simplified models, Appl. Therm. Eng. 73 (1) (Dec. 2014) 842–858, https://doi.org/10.1016/j.applthermaleng.2014.08.037.
[24] P. Merati, C. Davis, K.H. Chen, J.P. Johnson, Underhood buoyancy driven flow—an experimental study, J Heat Transfer 133 (8) (Aug. 2011) 1–9, https://doi.org/10.1115/1.4003758/467382.
[25] K.H. Chen, J. Johnson, P. Merati, C. Davis, Numerical investigation of buoyancy-driven flow in a simplified underhood with open enclosure, SAE International Journal of Passenger Cars - Mechanical Systems 6 (2) (2013) 805–816, https://doi.org/10.4271/2013-01-0842.
[26] Z. Wang, J. Han, D. Mukutmoni, Numerical simulation of unsteady natural convection in a simplified engine bay enclosure under soak conditions, in: *SAE Technical Papers*, SAE International, 2014, https://doi.org/10.4271/2014-01-0651.
[27] B.B. Minovski, L. Lofdahl, P. Gullberg, Numerical investigation of natural convection in a simplified engine bay, in: SAE Technical Papers, SAE International, Apr. 2016, https://doi.org/10.4271/2016-01-1683.
[28] B. Minovski, L. Löfdahl, J. Andrić, P. Gullberg, A coupled 1D–3D numerical method for buoyancy-driven heat transfer in a generic engine bay, Energies 2019 (21) (Oct. 2019) 4156 https://doi.org/10.3390/en12214156, 12, Page 4156, vol. 12.
[29] M. Khaled, et al., Experimental study of the flow induced by a vehicle fan and the effect of engine blockage in a simplified model, Int. J. Automot. Technol. 17 (4) (Aug. 2016) 617–627, https://doi.org/10.1007/S12239-016-0061-6.
[30] R. Franzke, S. Sebben, E. Willeson, Experimental Investigation of the Air Flow in a Simplified Underhood Environment, vol. 236, Nov. 2021, pp. 2272–2282 https://doi.org/10.1177/09544070211059786, 10–11.
[31] B. Sweetman, I. Schmitz, B. Hupertz, N. Shaw, J. Goldstein, Experimental and numerical investigation of vehicle drive and thermal soak conditions in a simplified engine bay, SAE International Journal of Passenger Cars - Mechanical Systems 10 (2) (Mar. 2017) 433–445, https://doi.org/10.4271/2017-01-0147.
[32] INTAB Interface-Teknik AB, PC-logger 2100 User's Manual, 2004.
[33] Siemens Digital Industries Software, Simcenter STAR-CCM+ User Guide, 2023 version 2302.
[34] Cartridge heaters." Accessed: November. 23, 2023. [Online]. Available: https://ihpheating.com/cartridge-heaters-750c/.